

Winds of Massive Stars: High Resolution X-ray Spectra of Stars in NGC 3603

DAVID P. HUENEMOERDER,¹ NORBERT S. SCHULZ,¹ AND JOY S. NICHOLS²

¹*Massachusetts Institute of Technology*

77 Massachusetts Ave.

Cambridge, MA 02139, USA

²*Harvard-Smithsonian Center for Astrophysics*

60 Garden St.

Cambridge, MA 02138, USA

ABSTRACT

The cluster NGC 3603 hosts some of the most massive stars in the Galaxy. With a modest 50 ks exposure with the Chandra High Energy Grating Spectrometer, we have resolved emission lines in spectra of several of the brightest cluster members which are of WNh and O spectral types. This observation provides our first definitive high-resolution spectra of such stars in this nearby starburst region. The stars studied have broadened X-ray emission lines, some with blue-shifted centroids, and are characteristic of massive stellar winds with terminal velocities around 2000–3000 km s⁻¹. X-ray luminosities and plasma temperatures are very high for both the WNh and O stars studied. We conclude that their X-rays are likely the result of colliding winds.

Keywords: stars: Wolf-Rayet — stars: massive — stars: individual (HD 97950, MTT 68, MTT 71, Sher 47) — X-rays: stars

1. INTRODUCTION

The starburst phenomenon is an influential process in the evolution of stellar systems. The formation of massive stars can have a profound effect on their environment through ionizing radiation, kinetic energy of massive winds, and ultimately supernovae explosions. NGC 3603 is a relatively nearby galactic starburst region, close enough that individual stars can be observed in detail. It is well recognized as an important cluster in relation to the similar but more distant R136a association, the much more active Arches cluster, and the distant powerhouses in starburst galaxies.

Mass loss rates and compositions can be determined through high-resolution spectroscopy. In X-rays, we can characterize emission mechanisms, discriminating between wind-shocks, magnetic confinement, or colliding winds. X-ray emission line strengths and shapes are key diagnostics of wind structure.

Some early *Chandra* observations of hot stars challenged the canonical wind-shock models (Gagné et al. 2005; Schulz et al. 2003) when some massive stars, such as θ^1 Ori C were found to have narrow lines and high temperatures. Gagné et al. (2005) successfully applied a magnetically confined wind model to the θ^1 Ori C spectra, and this is now largely accepted as an explanation for narrow lines in hot stars. Other stars, such as ζ Pup do show wind-broadened profiles (Cassinelli et al. 2001; Kahn et al. 2001; Kramer, Cohen & Owocki 2003). The wind-shock models for single stars do not predict the high plasma temperatures seen in some stars. In binary systems, colliding winds can lead to high temperatures since the temperature

is proportional to the square of the wind velocity (Luo, McCray & Mac Low 1990; Stevens, Blondin & Pollock 1992).

NGC 3603 is the closest starburst cluster at a distance of ~ 7.6 kpc and an age of about 1–3 Myr (Melena et al. 2008; Stolte et al. 2006; Hofmann, Seggewiss & Weigelt 1995). Stolte et al. (2006) compared NGC 3603’s central Young Cluster (YC) to other clusters and note that it has a similar core radius to the Orion Nebular Cluster (ONC) of about 0.2 pc, and even a similar stellar number density of about $2 \times 10^4 \text{ pc}^{-3}$, but its mass density of $1 \times 10^5 M_{\odot} \text{ pc}^{-3}$ is 5 times that of the ONC; the NGC 3603 YC core mass equals the entire mass of the ONC. The Arches cluster has somewhat higher mass and mass density than NGC 3603 YC; R136 is very similar to NGC 3603 in many ways (Moffat, Drissen & Shara 1994; Stolte et al. 2006). Hence, the NGC 3603 Young Cluster represents an important object to study among others as, in the words of Stolte et al. (2006), it “*provides a resolved template for extragalactic star-forming regions.*”

The stars in the core of NGC 3603 are collectively known as HD 97950 and also WR 43. Moffat, Seggewiss & Shara (1985) first identified the central unresolved object as multiple WN-type stars. Hofmann, Seggewiss & Weigelt (1995) resolved the stellar core of NGC 3603 into 28 stars using speckle interferometry. These stars reside in a central $6 \times 6 \text{ arcsec}^2$ field (at 7.6 kpc, 6 arcsec corresponds to 0.22 pc). They identified several of the components as late WN or Of stars. Crowther & Dessart (1998) conducted a spectroscopic analysis of the core stars in NGC 3603 and determined their fundamental properties. HD 97950 was resolved into several different components, and three of them, A1, B, and C, have been classified as WN6h+abs types — nitrogen-rich Wolf-Rayet stars with substantial abundance of hydrogen; they have not evolved past hydrogen-core burning. Melena et al. (2008) obtained spectra of NGC 3603 stars, determining characteristics for 16 additional objects; they also compared to many of the previous results. The three WN stars’ winds contribute about 65% of the cluster kinetic energy, which is more than that from cluster’s 20–30 other O-stars combined (Crowther & Dessart 1998).

In the ACIS image data analyzed by Moffat et al. (2002), source C was the brightest in X-rays. HD 97950-C is a WN6h+abs type, with $L/L_{\odot} \sim 10^6$, $M/M_{\odot} \sim 62$, $\dot{M} \sim 10^{-4} M_{\odot} \text{ yr}^{-1}$, and a terminal wind velocity of 2500 km s^{-1} (Crowther & Dessart 1998). It is also a single-lined spectroscopic binary (Schnurr et al. 2008) with a period of 8.9 days and a velocity amplitude of 200 km s^{-1} .

The Wolf-Rayet (WR) stellar class contains some of the most massive and luminous stars. Their dense, high velocity stellar winds, and ultimate supernova explosion significantly affect the composition and dynamics of the interstellar medium. They are important in galactic feedback and can alter the environment in their host star cluster. There is some evidence that the X-ray production in WR stars is perhaps different from known O-star mechanisms of wind-shocks, which are thought to occur near the stellar photosphere in the wind acceleration zone, or from magnetically confined winds, in which strong magnetic fields constrain the winds. High-resolution X-ray spectra of WR 6 (EZ CMa), from *XMM-Newton*-Newton RGS and from *Chandra*/HETG spectrometers showed that the X-rays are generated far out in the wind (Oskinova et al. 2012; Huenemoerder et al. 2015). The X-ray emission mechanism is not known. Hence, more high resolution spectra of very massive stars are required to further study winds in this regime. The central cluster of NGC 3603 provides us with an opportunity to study in detail some of the most massive stars in the Galaxy.

2. OBSERVATIONS AND CALIBRATION

Using the *Chandra*/HETG spectrometer (Canizares et al. 2005), we observed NGC 3603 in 2011 for 47 ks (observation ID 13266). The HETGS spectra cover the range from about 1–30 Å, as dispersed by two types of grating facets, the High Energy Grating (HEG) and the Medium Energy Grating (MEG), with

Table 1. Properties of Selected NGC 3603 Members

| Star | Spectral Type | Binarity, Period (d) | Mass (M_{\odot}) | $L_{\text{bol}}^{\text{a}}$ ($10^6 L_{\odot}$) | v_{∞} (km s^{-1}) | γ (km s^{-1}) | K (km s^{-1}) | f_{x}^{b} ($\text{ergs cm}^{-2} \text{s}^{-1}$) |
|---------|---------------|----------------------|----------------------|--|-------------------------------------|---------------------------------|----------------------------|---|
| A1 | WN6h + WN6h | SB2, 3.77 | 116, 89 | 4.0 | 2700 | 153 | 330, 433 | 5.74×10^{-13} |
| A2 | O3 V | - | - | 1.2 | - | - | - | - |
| A3 | O3 III (f*) | - | - | 0.8 | - | - | - | - |
| B | WN6h | single | 89 | 2.9 | 2700 | 167 | - | 2.69×10^{-13} |
| C | WN6h+? | SB1, 8.9 | 62 | 2.2 | 2500 | 186 | 200 | 1.08×10^{-12} |
| MTT 68 | O2 If* | vis., 0.38'' | 150 | 0.4 | - | - | - | 1.28×10^{-12} |
| MTT 71 | O4 III | - | 80 | 1.5 | - | - | - | 2.46×10^{-13} |
| Sher 47 | O4 IV (f) | - | - | 0.5 | - | - | - | 3.53×10^{-13} |

NOTE—Designations A-B-C refer to the sub-components of HD 97950.

Data sources: [Drissen et al. \(1995\)](#); [Crowther & Dessart \(1998\)](#); [van der Hucht \(2001\)](#); [Melena et al. \(2008\)](#); [Schnurr et al. \(2008\)](#); [Crowther et al. \(2010\)](#); [Roman-Lopes \(2013\)](#); [Roman-Lopes, Franco & Sanmartim \(2016\)](#); [Maíz Apellániz et al. \(2016\)](#).

^aLuminosities for A1, B, and C are from [Crowther et al. \(2010\)](#); others are from [Crowther & Dessart \(1998\)](#) but re-scaled to a distance of 7.6 kpc (from their value of 10.1 kpc).

^bFlux is the total band (0.5–8.0 keV) from [Townsley et al. \(2014\)](#), with a caveat that these were significantly saturated by CCD event pile-up.

resolving powers ranging from 100 to 1000 and approximately constant full-width-half-maxima ($FWHM$) of 12 mÅ for HEG and 23 mÅ for MEG. Our observation was designed as a “snapshot”, just long enough to characterize the strongest emission lines of the brightest members, based on the low-resolution ACIS observations.

The *Chandra* data were reprocessed with standard Chandra Interactive Analysis of Observations (CIAO) programs ([Fruscione et al. 2006](#)) to apply calibration data appropriate to the epoch of observation (primarily CIAO 4.6 and the corresponding calibration database, version 4.5.9, though some recent reprocessing was done with CIAO 4.10 and CALDB 4.7.8).¹ The counts spectra are composed of four orders per source per observation: the ± 1 orders for each grating type, the MEG and HEG, which have different efficiencies and resolving powers. The default binning over-samples the instrumental resolution by about a factor of four.

Observation-specific calibration files are required for analysis to convolve a model flux spectrum with the instrumental response to produce model counts. CIAO programs were used to make the effective areas (“Auxiliary Response File”, or ARF) and the spectral redistribution and extraction-aperture efficiency files (“Response Matrix File”, or RMF) for each spectral order for each source (see [Davis 2001](#), for a detailed definition of the response).

To extract spectra of multiple sources, we need to customize source positions and extraction regions to minimize confusion. In [Figure 1](#) we show X-ray images of the field at successively decreasing scales. In

¹ Some recent calibration updates have retroactive changes in the effective area of order 5% at 12 Å due to revisions in the contamination model. There are no other significant differences in recent (post observation epoch) CIAO versions which affect event processing, spectral extraction, or line characteristics. For these data and our purposes, the effective area revisions are not important, so we have not re-extracted and re-fit data with the most recent calibrations.

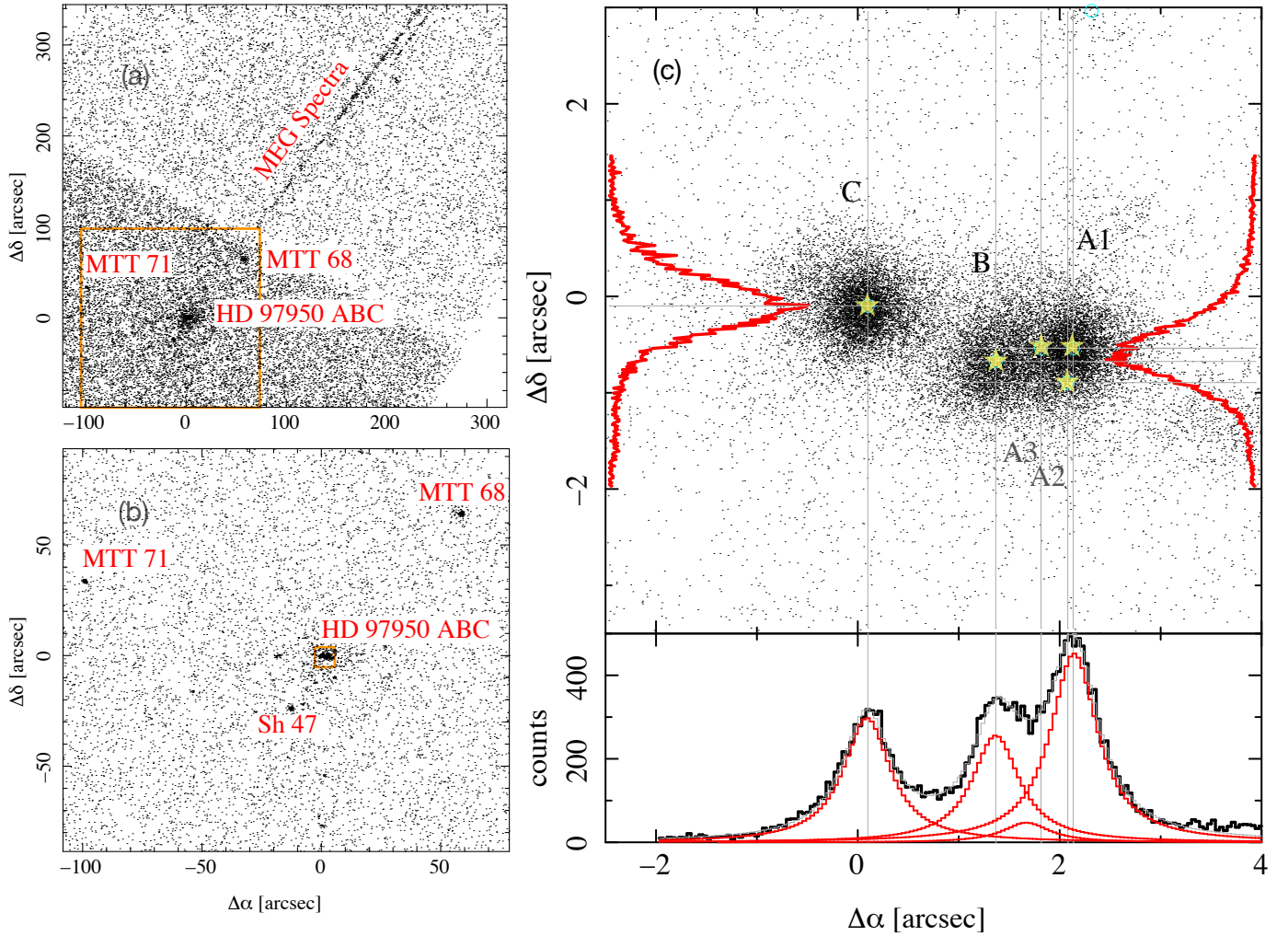


Figure 1. Images of the field for decreasing scales. The top left panel is a large-scale view with the cluster core in the lower left and the MEG spectrum running diagonally to the upper right. The lower left is an expanded scale. The left panels are from the HETG observation (observation ID 13266). The right panel shows the deeper ACIS-I data (ObsIDs 12328, 12329), which better shows the event distribution of the HD 97950 core. Known star positions are marked, and marginal histograms along the axes show the X-ray event distributions (y -scales for the upper-panel marginal histograms are arbitrary). Positions of the components are from [Drissen et al. \(1995\)](#). For the y -axis histograms, we have separated events for C from A1-B. In all panels, east is left and north is up.

the rightmost panel, we overlay positions of the optical components from [Drissen et al. \(1995\)](#). Properties of objects relevant to this study are given in Table 1.

From the marginal histograms, we can see that the X-rays in the core are dominated by components A1, B, and C, and that in this observation, C is fainter than A1. The dispersion direction is roughly diagonal, and the MEG trace of A1+B can be seen faintly in the upper-left panel of Figure 1 extending to the upper right, along with the bright sources MTT 68 at about 1.4 arcmin northwest of the core ([Melnick, Tapia & Terlevich 1989](#); [Roman-Lopes 2013](#)), and MTT 71 at about 1.7 arcmin northeast of the core. The HETG resolution is not affected by off-axis angles below $2'$.

We used MARX² (Davis et al. 2012) to simulate the field and to assess source confusion in detail. While components A1 and B are marginally resolved in zeroth order, they are not in the dispersed spectrum, due to the additional grating astigmatic profile in the cross-dispersion direction. The wavelength offset between A1 and B, projected along the MEG direction, is 1.46 pixels (0.016 Å), or about 800 km s⁻¹ at 6 Å. With the extraction centered on A1, combination of positive and negative orders would in principle result in B’s contributions being offset by ± 800 km s⁻¹ then summed with A1. However, A1 is twice as bright as B, and using a narrow extraction region reduces B’s contribution further, as does including the well separated HEG spectra. Experiments in fitting faked data with offsets showed that line centroids are unaffected (as expected), but the line shapes become a bit flatter. Even with some broadening due to confusion, we will see in Section 3 that the line widths are still much larger than we expect from source confusion.

In Figure 2, we show cross-dispersion profiles as fit to MARX simulations, using the 6–10 Å region of the MEG spectrum of the A1+B extraction. The counts in the A1 extraction region in the MEG arm alone is about 60% from A1.

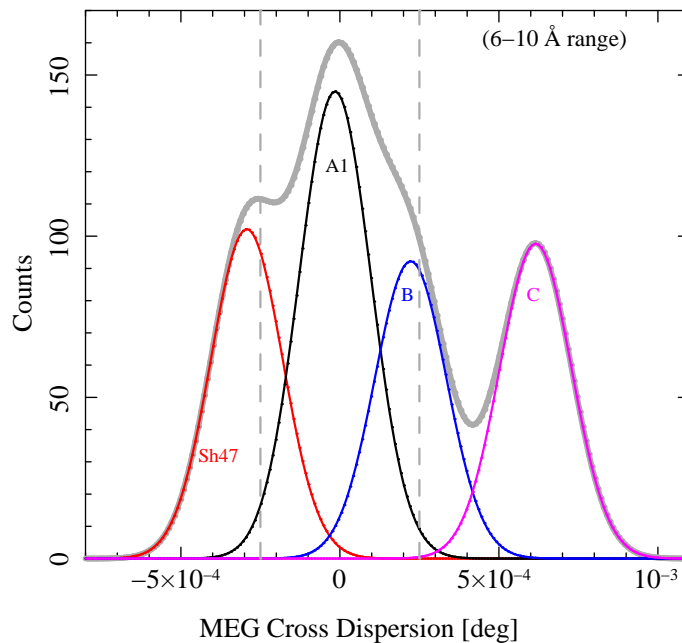


Figure 2. Cross-dispersion profiles for the A1+B extraction in the 6–10 Å range of the MEG order, from MARX simulations. Vertical dashed lines show the limits of the extraction region for A1, which includes tails of Sh 47 and B.

We also analyzed MTT 68, MTT 71, and Sher 47. The latter, however, is aligned with the A1+B MEG spectrum, so its MEG spectrum is not useful. In turn, its MEG counts contaminate the A1+B spectrum, though it is offset enough, by 0.63 Å, that any emission lines will not overlap those of A1+B. It is somewhat fainter—we estimate that Sh 47 could contribute about 12% of the A1+B HEG plus MEG counts spectrum. As a further test of confusion from Sh 47, we can compare the HEG and MEG flux of A1+B, which should differ if Sh 47 contaminates the MEG arm, and we can look for offset spectral features. In Figure 3, we show the HEG and MEG fluxes³ for the A1+B extraction. The fluxes agree, and there are no features at

² <http://space.mit.edu/cxc/marx>

³ Flux spectra are derived by dividing by the counts expected for a flat spectrum, that is, by the integral over the response. This is an approximation to the flux, but still includes the instrumental broadening. This was done in the ISIS analysis package, and full details are given in the manual (see <http://space.mit.edu/cxc/software/isis/manual.pdf#page.76>).

the expected offsets. Hence, we conclude that the limited extraction region widths and order-sorting have mitigated the contributions from Sh 47.

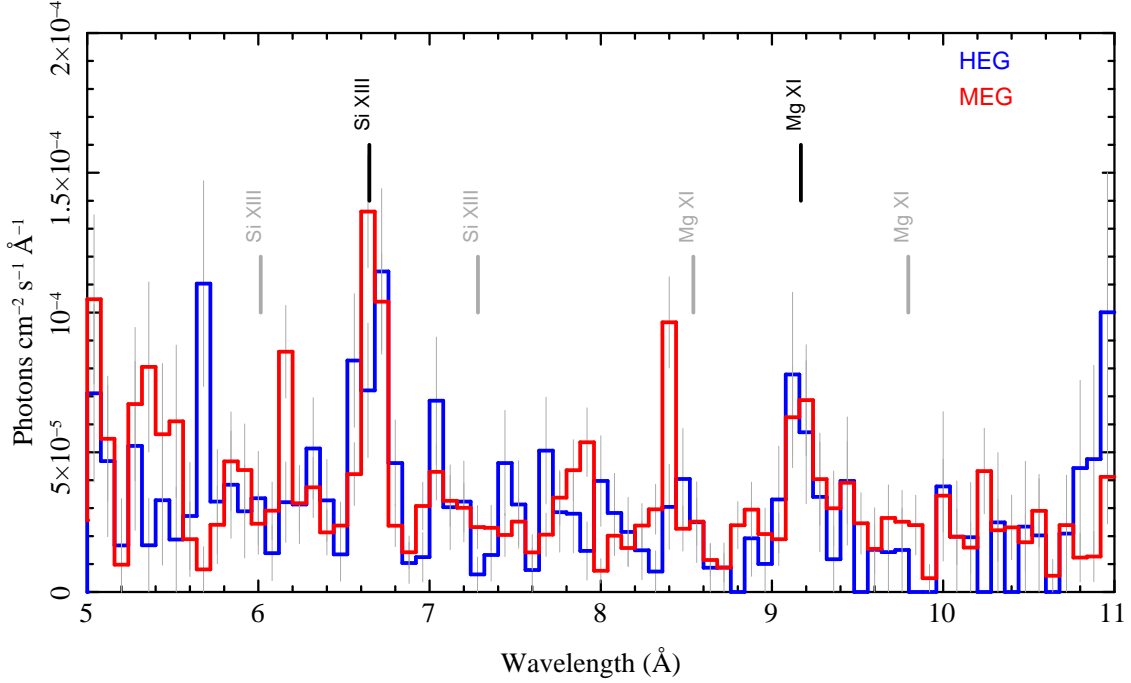


Figure 3. The A1+B flux spectra for HEG (blue) and MEG (red), each of which have positive and negative orders combined. If Sh 47 significantly contaminated the MEG spectrum of A1+B, the HEG and MEG fluxes would not agree. We also see no significant emission features at the expected positions for the Sh 47 spatial offset; we mark the strongest expected lines of Si XIII and Mg XII for the A1+B extraction scale in black, and to either side in gray, where Sh 47 confusing lines would be. Spectra have been binned to $0.08 \text{ \AA}/\text{bin}$.

In Figure 4, we show the combined flux spectra for the HEG and MEG first orders of components A1+B, C, MTT 68, and MTT 71. Count rates and fluxes (which are largely model-independent) are given in Table 2.

In this relatively short, single pointing, we cannot totally mitigate source confusion. In the future, we hope to obtain deeper exposures at multiple roll angles which will allow us to better extract unconfused spectra.

We have examined the background rate by extracting the relatively isolated MTT 68 with standard width spatial masks, which provide 10 times the width of the source region for spectrally-adjacent background regions. The rate is less than about $10^{-4} \text{ cts s}^{-1} \text{ \AA}^{-1}$ for standard extraction regions, and is negligible for the grating spectral analysis.

We have not included zeroth orders in our analysis. While the HETG zeroth order effective area exceeds that of the combined first orders above 2 keV (below 6 \AA) by up to a factor of 3 (with a median factor of 1.6), there are uncertainties in the calibration of order 5–10% between zeroth and first orders. Furthermore, we would require small extraction regions for the close sources, C, B, and A1 and the aperture correction introduces another potentially larger systematic uncertainty. As can be seen from inspection of the counts below 6 \AA in Figure 4, we do have enough signal in the dispersed spectrum for characterization of the highest temperature plasmas. Since we will be primarily interested in the resolved emission lines, we will not further consider the zeroth order in our analysis.

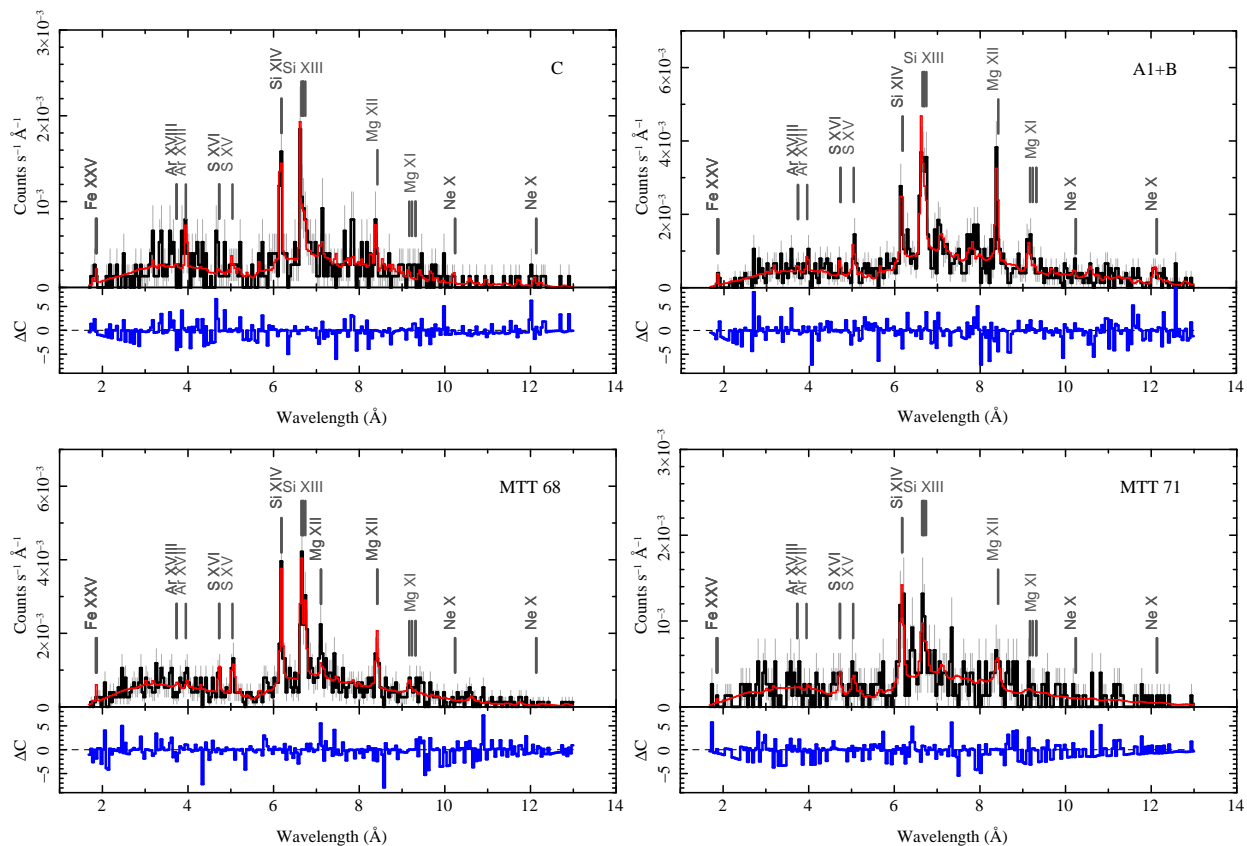


Figure 4. Summary HETGS counts spectra: combined HEG and MEG first orders. The locations of some spectral features, primarily H- and He-like ions, are marked. The red curve is a two-temperature AtomDB (Foster et al. 2012) model from a global fit, whose scaled residuals (as the C -statistic) are shown in the lower portion of each panel.

3. SPECTRAL MODELING

To characterize the spectra, we fit two temperature, foreground absorbed AtomDB (Foster et al. 2012) plasma emissivity models.⁴ This is not meant to imply that this is an appropriate physical model for the X-ray emission from a stellar wind. A wind is accelerating and possibly stratified: emission can originate from regions of different velocities, temperatures, and overlying continuum absorption optical depths. Winds can also be clumped. These all affect the X-ray energy distribution and line profiles (Owocki & Cohen 2001; Oskinova, Feldmeier & Hamann 2004; Cohen et al. 2014). Instead, our intent is to provide a simple characterization of the emitting plasma appropriate to the quality of the data, and to measure emission line parameters which are independent of global plasma models.

Because of the heavy foreground absorption of about 10^{22} cm^{-2} (Townsend et al. 2014; Romano et al. 2008; Moffat et al. 2002), we are not sensitive to cooler plasma temperatures of a few MK. Since we see emission lines of Si and Mg, we have temperatures near 10 MK, and the continuum present between 2–6 Å indicates temperatures in the tens of MK, hence a $2T$ model should suffice for general characterization of the plasma model. In addition to foreground absorption, there could be intrinsic absorption within the stellar wind itself, hence, we let the column be fit.

⁴ The atomic database, AtomDB (www.atomdb.org), is produced by the *Astrophysical Plasma Emission Code*, or APEC, which is also commonly referred to as the *Astrophysical Plasma Emission Database*, or APED. These are often used interchangeably when referring to spectral emissivity models derived from APEC.

Table 2. Source Rates for Selected NGC 3603 Members

| Object | r_0 | $r_{\pm 1}$ | f_x |
|----------------------|-------|-------------------|-------------------|
| A1 | 8.84 | – | – |
| B | 4.72 | 26.0 ^a | 1.31 ^a |
| C | 6.81 | 9.47 | 0.66 |
| MTT 68 | 15.33 | 22.0 | 1.37 |
| MTT 71 | 4.58 | 9.32 | 0.51 |
| Sher 47 ^b | 7.49 | 3.65 | 0.63 |

^aHETGS dispersed spectral rates are for A1+B.

^bFirst orders and flux are from HEG only.

NOTE— Rates for zeroth order (r_0) and $\pm 1^{\text{st}}$ orders ($r_{\pm 1}$) are given in cts ks^{-1} .

Flux in the dispersed spectra, f_x , is in $10^{-12} \text{ ergs cm}^{-2} \text{ s}^{-1}$, using the model evaluated over 1–40 Å.

Since the emission lines are of primary interest, we also fit a global “turbulent” broadening parameter (i.e., constant velocity width), and a Doppler shift. These allow us to characterize the line width and apparent offset of the centroid, which might be due to skewness of the profile (see for example [Owocki & Cohen 2001](#)).

Finally, we also allowed elemental abundances for Fe, Ar, S, Si, Mg, and Ne to be free. While these parameters are related to the physical abundances, they also compensate for systematic errors in plasma temperatures as per limitations of the adopted two-component model. We modified the [Asplund et al. \(2009\)](#) appropriately for the depleted H fraction of WNh stars given by [Crowther & Dessart \(1998\)](#) in which the H to He number ratio is 6, or by mass fraction, 0.59 H.⁵ Only the relative abundances of Mg, Si, and Fe are reasonably constrained, since they have the strongest or most numerous (in the case of Fe) lines.

We fit the 1.7–13 Å region using a Powell minimization method and a Cash (maximum likelihood) statistic. These global fits and residuals are shown in Figure 4. Model parameters are given in Tables 3 and 4. Fluxes of the models, since they characterize the empirical shape of the observed spectrum (and are largely model independent), are given in Table 2. Luminosities, which depend critically on assumed absorption (here all assumed in the foreground) are given in Table 3, using a distance of 7.6 kpc ([Melena et al. 2008](#)).

In addition to using Gaussian profiles, we used a simple analytic profile characteristic of asymptotic flow of thick wind ([Ignace 2001](#)) as successfully applied to the HETGS spectrum of the Wolf-Rayet star, WR 6 ([Huenemoerder et al. 2015](#)). This profile has two shape parameters, the terminal velocity (v_∞), and a shape, $q > -1$; $q = 0$ is the nominal wind expansion model which creates a “shark-fin” shaped profile; $q = -1$

⁵ In the usual by-number decimal logarithmic scale in which the hydrogen abundance is 12, the WNh abundances of the elements relevant here are He = 11.22, Ne = 8.02, Mg = 7.69, Si = 7.60, S = 7.21, Ar = 6.49, and Fe = 7.59.

Table 3. Spectral Model Parameters

| Object | N_H | σ_{lo} | σ_{hi} | T_1 | σ_{lo} | σ_{hi} | T_2 | σ_{lo} | σ_{hi} | EM_1 | σ_{lo} | σ_{hi} | EM_2 | σ_{lo} | σ_{hi} | L_x^a | $\log(L_x/L_{bol})$ |
|----------------------|--------------------------------------|---------------|---------------|-------|---------------|---------------|-------|---------------|---------------|--------------------------------------|---------------|---------------|--------------------------------------|---------------|---------------|--|---------------------|
| | (10 ²² cm ⁻²) | | | (MK) | | | (MK) | | | (10 ⁵⁶ cm ⁻³) | | | (10 ⁵⁶ cm ⁻³) | | | (10 ³⁴ ergs s ⁻¹) | (dex) |
| A1+B | 1.3 | 0.9 | 1.9 | 8.7 | 6.4 | 9.5 | 36.5 | 27.9 | 48.2 | 8.0 | 4.9 | 13.2 | 4.4 | 3.5 | 5.6 | 3.60 | -5.8 |
| C | 2.6 | 1.9 | 3.0: | 12.1 | 10.7 | 13.4 | 92.1 | 40.5 | 100: | 5.3 | 2.7 | 9.0 | 1.2 | 0.8 | 2.1 | 2.59 | -5.5 |
| MTT 68 | 1.5 | 1.2 | 2.1 | 10.8 | 9.0 | 12.6 | 60.7 | 43.5 | 100: | 2.9 | 1.7 | 7.0 | 4.3 | 3.3 | 5.3 | 2.17 | -4.8 |
| MTT 71 | 0.8 | 0.8 | 1.5 | 12.6 | 7.3 | 18.6 | 50.2 | 33.0 | 100: | 0.7 | 0.2 | 3.0 | 1.8 | 0.9 | 2.4 | 0.60 | -6.0 |
| Sher 47 ^b | 1.0: | — | — | 6.9 | 2.8 | 11.1 | 27.6 | 22.1 | 35.8 | 1.2 | 0.3 | 5.9 | 3.2 | 2.5 | 4.0 | 1.20: | -5.2: |

^a Assumes a distance of 7.6 kpc.

^b Only the HEG spectrum was fit, and the value of N_H was assumed.

NOTE—Columns labeled σ_{lo} , σ_{hi} are the 90% confidence limits for the preceding parameter. A colon (“:”) indicates an uncertain value, as in an error limit which did not converge. The model fit was of the form (AtomDB(1) + AtomDB(2)) * PHABS(1).

Table 4. Spectral Model Parameters: Relative Abundances

| Object | Ne | σ_{lo} | σ_{hi} | Mg | σ_{lo} | σ_{hi} | Si | σ_{lo} | σ_{hi} | S | σ_{lo} | σ_{hi} | Ar | σ_{lo} | σ_{hi} | Fe | σ_{lo} | σ_{hi} |
|--------|-----|---------------|---------------|-----|---------------|---------------|-----|---------------|---------------|-----|---------------|---------------|-----|---------------|---------------|-----|---------------|---------------|
| AB | 1.7 | 0.6 | 3.9 | 0.9 | 0.6 | 1.4 | 1.1 | 0.7 | 1.7 | 1.5 | 0.7 | 2.8 | 2.8 | 0.1 | 6.6 | 0.9 | 0.4 | 1.9 |
| C | 6.6 | 0.8 | 6.6 | 0.6 | 0.2 | 1.3 | 1.1 | 0.6 | 1.8 | 0.4 | 0.1 | 1.5 | 5.1 | 1.3 | 6.6 | 1.7 | 0.7 | 3.3 |
| MTT68 | 0.1 | 0.1 | 3.8 | 1.3 | 0.7 | 2.2 | 2.5 | 1.3 | 3.3 | 3.3 | 1.4 | 3.3 | 1.5 | 0.1 | 6.6 | 0.9 | 0.3 | 1.6 |
| MTT71 | 0.3 | 0.1 | 5.0 | 1.0 | 0.2 | 2.6 | 2.5 | 0.9 | 3.3 | 3.1 | 0.6 | 3.3 | 0.1 | 0.1 | 6.6 | 0.3 | 0.1 | 1.0 |

NOTE—Abundances are by number fraction relative to the WNh values of [Crowther & Dessart \(1998\)](#). Columns labeled σ_{lo} , σ_{hi} are the 90% confidence limits for the preceding parameter. Only Mg, Si, and Fe are reasonably constrained. The others are listed only because they are formal values of the fit. Sh 47 is not included because it had too weak a spectrum to fit abundances, which were assumed to be 1.0.

results in a flat-topped profile (as would be emitted by a physically thin expanding shell; and $q > 0$ becomes increasingly steep, rapidly falling from the sharp blue wing at $-v_\infty$ (see [Huenemoerder et al. \(2015\)](#) for example profiles and the analytic functional form). This line model was *not* allowed to have a free Doppler shift; line centers were instead frozen at their relatively small line-of-sight velocities.

All fitting and modeling was done using the *Interactive Spectral Interpretation System* (ISIS⁶; [Houck & Denicola \(2000\)](#)), which provides interfaces to AtomDB and Xspec models.

In Figure 5 we show the Si XIV to Si XIII region twice, once fit with the AtomDB models using Gaussian profiles, and again as fit with the asymptotic thick wind profiles. The wind-profile is convenient because it clearly delimits the maximum extent of the blue wing, but we cannot claim that it is better than a Gaussian for these stars. Our general qualitative impression is that it seems to better match Si XIV than a Gaussian.

Figures 6–7 show the confidence contours (90% limits) for the interesting shape parameters for the Gaussian and wind-profile models respectively. For the Gaussian, Doppler-shifted fits, we corrected for our mean line-of-sight velocities, as well as they are known (see Table 1), and mark the expected velocity range of the

⁶ <http://space.mit.edu/cxc/software/isis>

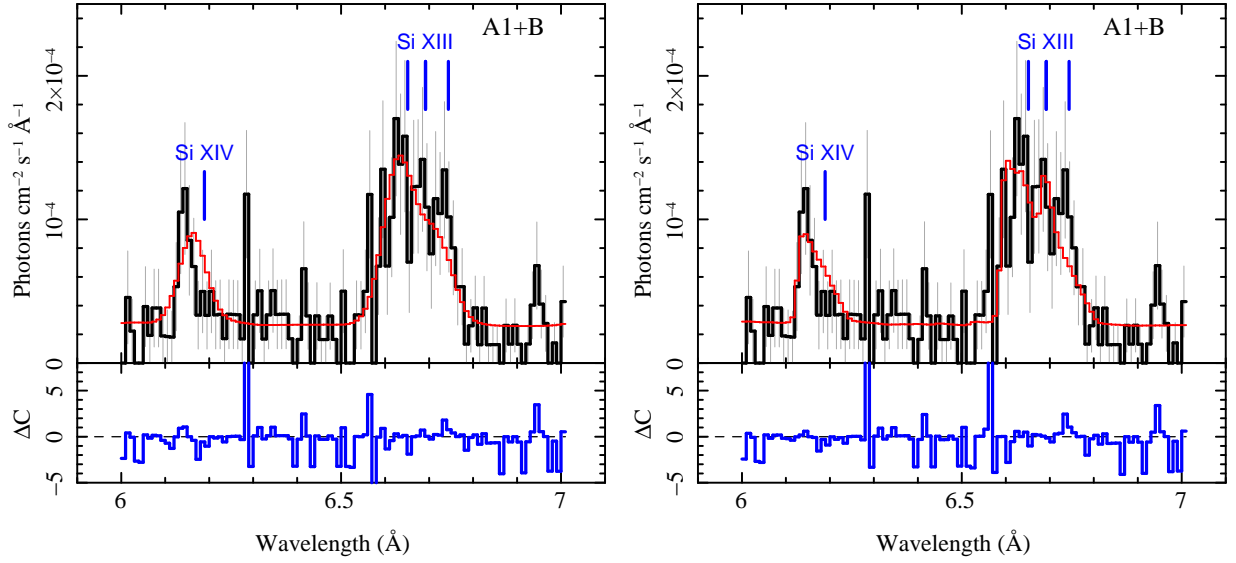


Figure 5. Gaussian (left) and wind (right) profile AtomDB plasma fits to the to A1+B spectra. Black are the observed counts for the combined HEG and MEG first orders. The red curve is the AtomDB model with Doppler shifted, Gaussian-broadened (left), or an asymptotic wind (right) profile. The Si XIV H-like (6.18 Å) and Si XIII He-like lines (6.65, 6.69, and 6.74 Å) rest wavelengths are marked. The Si lines are broader than instrumental, and also have a blueshifted centroid.

single and double-lined binary systems (A1 and C). Best fits and corresponding 90% errorbar values shown in Figures 6–7 are listed in Table 5.

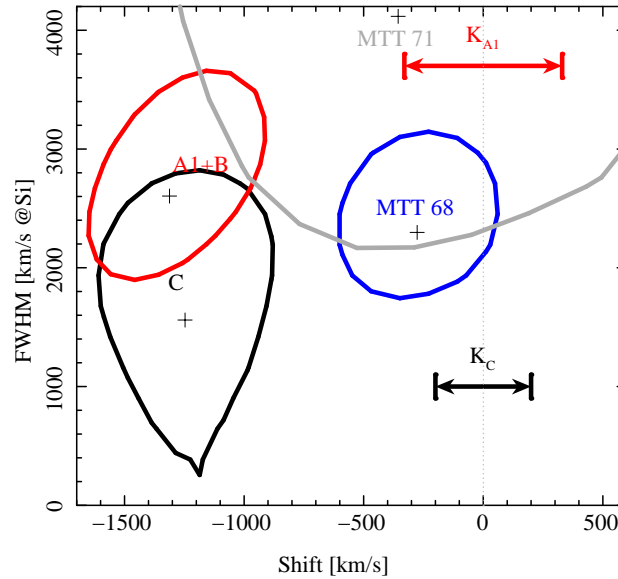


Figure 6. Gaussian-broadened, AtomDB fits to the 1.7–13 Å region, confidence contours of centroid vs line width (90% contours). K_x denotes the expected velocity amplitude of the binaries, A1 and C. Since the Doppler shifts are much larger than radial velocity amplitudes, they are due to line asymmetry, not orbital motion. MTT 68 is unshifted, and so is likely due to a thinner wind. MTT 71 is poorly constrained, but does have broadened lines.

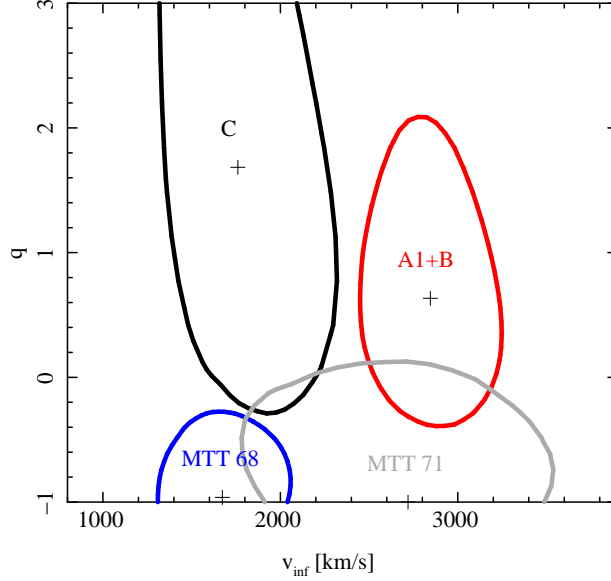


Figure 7. Asymptotic wind profile fits, confidence contours of v_∞ and the shape parameter, q (90% contours). Fits were constrained to the Si XIV–Si XIII region.

Table 5. Line Fit Parameters

| Object | v_∞ (km s^{-1}) | σ_{90} ^a | $FWHM$ (km s^{-1}) | σ_{90} |
|--------|--------------------------------------|----------------------------|----------------------------------|---------------|
| A1+B | 2845 | 400 | 2603 | 932 |
| C | 1760 | 461 | 1560 | 1200 |
| MTT 68 | 1672 | 371 | 2298 | 684 |
| MTT 71 | 2719 | 870 | 4117 | 1945 |

^aThe approximate one-sided 90% confidence limit, as measured from the 90% contours shown in Figures 6–7.

4. X-RAY LIGHT CURVES

We extracted light curves from the zeroth order and dispersed spectra for each of the stars studied. Figure 8 shows the count rates. In the zeroth orders, we can isolate stars A1 and B, so we show their zeroth orders individually, along with their sum and the blended count rate in dispersed light.

5. DISCUSSION

X-ray line emission can be a sensitive probe of the structure and energetics of stellar winds from massive stars. The wind temperatures and abundances can be determined from line and continuum emission. Wind radial structure can be determined from He-like triplet ratios which are strongly affected by UV photoexcitation. Wind dynamics can be revealed by X-ray line profiles. It is important that we obtain line

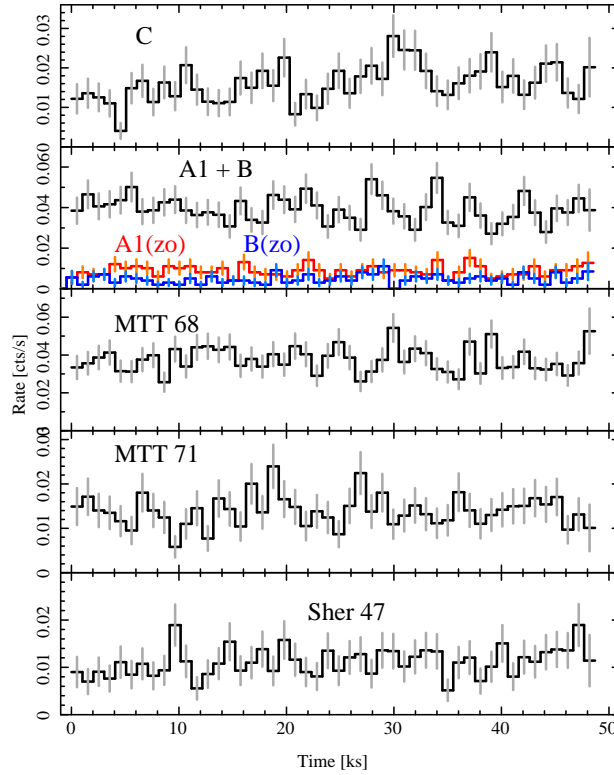


Figure 8. X-ray light curves of the selected stars with 1 ks bins. The black histogram in each panel shows the sum of the zeroth order and dispersed first orders count rates. Since stellar components A1 and B are combined in the dispersed spectrum, we also show their individual zeroth order curves. There is no obvious systematic or significant variability in any of the sources. One-sample Kolmogorov-Smirnov tests give probabilities of the curves being constant at their mean rate and normally distributed of 0.8 (C), 0.9 (A1+B), 0.9 (MTT 68), 0.6 (MTT 71), and 0.7 (Sher 47).

profile information on WN stars to understand the wind structure. While the central region of NGC 3603 is crowded, and two of the components (A1 and C) are binary systems, we have demonstrated that useful information can be obtained with the *Chandra*/HETG. Since our observation was relatively short, we cannot determine the emission line profiles’ shapes in detail, but we can reliably measure centroids and widths. Though there is some unresolvable spatial overlap among some sources, we can still obtain useful mean quantities.

HD 97950-C is not a single star, but its optical spectrum is dominated by the WN6h component, and a high mass ratio is implied (Schnurr et al. 2008). The relatively long period of 9 days also means that the companion is likely a later-type star, not a massive O-star. Hence, we expect the WR star to dominate the emission and we might not expect there to be a strong signature of colliding winds. The X-ray emission lines of HD 97950-C are significantly broadened, characteristic of $v_\infty \sim 1800 \text{ km s}^{-1}$, which is somewhat less than the value determined from UV lines (see Tables 1 and 5). The lines have a significantly blueshifted centroid (see Figure 6), indicating a strong wind signature of absorption on the red wing. The shift is much larger than is expected from any Doppler effect from binary orbital motion.

HD 97950-A1 is a double-lined binary, and is spatially confused with HD 97950-B in the HETG spectrum. Fortunately, all the components have the same spectral type of WN6h, so we can obtain mean parameters. HD 97950-A1 dominates, having a somewhat brighter zeroth order (Table 2); the rates of A1 and B are con-

sistent with 3 identical WN6h stars. These stars have a very high v_∞ of about 3000 km s^{-1} , but are consistent with the UV measurements at their 90% confidence levels. The lines, like component C, also have a significantly blueshifted centroid, larger than binary orbital motion could cause. The lines may have the “fin” shape characteristic of the asymptotic flow of an optically thick wind, but this is inconclusive and would require a much longer exposure to quantify. Some of the model profile mis-matches apparent in Figure 5 may simply be due to the wrong detailed profile shape. They may be more like the family of wind profiles derived by Owocki & Cohen (2001). We attempted parametric fitting (sum of Gaussians) of the Si XIII region shown in Figure 5, but while the fit statistic can be reduced, resulting line ratios are non-physical (e.g., forbidden-to-intercombination line ratios far above that allowed by standard plasma models). It could be that better spectra will support source-model-independent measurement and confirm such anomalies, but for the present analysis, we prefer the plasma-model based methods as a first characterization of these spectra.

MTT 68 is a very early-type star of spectral type O2 If* (Roman-Lopes 2013). It has an un-shifted but significantly broadened profile, as determined from the Gaussian profile fit (Figure 6). The “fin” profile fit is then forced to have a low q (more flat-topped) to make the line centered on its rest wavelength; this fit serves to characterize the wind velocity from the extent of the blue wing, to about 1700 km s^{-1} , but we prefer a Gaussian (or more weakly skewed) profile. This makes the wind likely different from the WNh stars’ winds.

MTT 71 also has an early spectral type, O4 III. It is fainter than MTT 68, so not as well characterized. We can confirm that its lines are broadened, with $v_\infty \sim 2700 \text{ km s}^{-1}$, though with large uncertainty. Whether the lines are shifted or non-Gaussian we cannot reliably determine.

Sher 47 (O4 IV(f)), was prominent in the field and had a visible dispersed spectrum. However, its MEG spectrum was confused with that of HD 97950-A1+B, so could not be used. There was not enough line signal in the HEG spectrum to warrant detailed line fits.

We expect winds with embedded shocks to be relatively cool in X-rays ($kT \lesssim 1 \text{ keV}$). Due to the high line-of-sight absorption, we cannot detect any very cool plasmas since the absorption hides the low temperature, long-wavelength component (above about 12 \AA or below about 1 keV). From the presence of strong Si and Mg lines, we know we have plasmas with $T \sim 10 \text{ MK}$. From presence of S, possibly Fe XXV, and the continuum, we know we have very high temperatures. These stars all have a rather hot plasma component, generally in excess of 50 MK , with comparable or even greater emission measure than the $\sim 10 \text{ MK}$ component (Table 3). This high temperature is also obvious via the continuum emission seen in the counts spectra in the $2\text{--}4 \text{ \AA}$ region (Figure 4). For comparison, WR 6 also has a high-temperature component of about 50 MK , but it has a much lower weight relative to the lower temperature plasmas. This is suggestive of colliding winds, though we don’t understand the origin of the 50 MK plasma far out in the wind of the single WR 6.

Colliding wind binaries can produce high temperature plasmas with quite diverse possible X-ray line profiles (Henley, Stevens & Pittard 2003), dependent upon the viewing geometry. Emission line skewness depends on the continuum optical depth and path length the wind collision region. Line emission can also have strong time dependence due to the changing aspect, density, and wind velocity in the collision region throughout the binary orbit.

It is likely that the X-ray emission from the stars we have investigated includes emission from colliding winds. Massive O and WR stars are known to be X-ray sources even as single stars, so colliding winds are an additional source of X-ray emission for these massive stars. Therefore it is difficult to determine if colliding winds are contributing to the X-ray emission of a source unless the data cover at least one full binary orbit,

in which case there may be variability in the light curve modulated by the orbit. Our observation is only about a half day out of the 3.77 d period for A1 and the 8.9 d period of C, so we cannot verify colliding winds in these objects.

We did examine the X-ray light curves (Figure 8), and all appear to be essentially constant. According to one-sample KS-tests assuming they are constant at their mean count rate, and with a variance in accordance with their mean counts, they have a high probability of being constant and normally distributed.

Two WR stars known to have some X-ray emission due to colliding winds (WR 140, Pollock et al. (2005); WR 25, Pollock & Corcoran (2006)) show strong variability in their X-ray light curves phased with their highly eccentric binary orbits. These are long-period systems and certainly unlike A1, B, or C in many regards, but they are relevant in showing the dramatic effect of wind collisions on X-ray luminosity, and the dependence on binary separation. Some WR stars with shorter periods are WR 46 ($P = 0.3$ d), or WR 6 ($P = 3.8$ d). While WR 46 is variable in the UV, it is not convincingly variable in X-rays (Zhekov 2012). WR 6 is variable in X-rays, but erratically, with small amplitudes over a day ($\sim 10\%$), up to a factor of 2 over a long term, but no convincing X-ray periodicity (Ignace et al. 2013). Our derived fluxes differ from those of Townsley et al. (2014) by up to a factor of two (see Tables 1 and 2), but their determinations are uncertain because the *Chandra*/ACIS imaging-mode data suffered from severe CCD count-rate saturation (“pile-up”; see Townsley et al. 2014, Table 4⁷). It is not conclusive whether our fluxes are indicative of long-term or orbital variability. While it is not unusual for stars like these to be constant in X-rays, longer term observations will be required to better detect and characterize any trends with orbital phase or epoch of observation.

These stars have large X-ray luminosities, in excess of 10^{34} ergs s⁻¹, which is also high relative to their bolometric luminosities, having $L_x/L_{\text{bol}} > 10^{-6}$. This strongly suggests that colliding winds are contributing to the X-ray emission of these stars. Components A1 and C are known to be binaries. The extreme stellar density of the region implies a high likelihood of multiplicity for all of these stars. In general, binary WR stars are more X-ray-luminous than single WR stars, having $L_x/L_{\text{bol}} > 10^{-7}$ (Stevens, Corcoran & Moffat 2002). WR binaries have a range of $\log(L_x/L_{\text{bol}})$ of -7.3 to -4.0 (Gagné et al. 2012). Specifically, the two previously mentioned known colliding wind binaries, WR 140 and WR 25, have $\log(L_x/L_{\text{bol}})$ of -4.8 and -5.5 , respectively. For comparison, the single Wolf-Rayet star, WR 6 (type WN4) has a luminosity 10–20 times lower than the stars studied here, and has $L_x/L_{\text{bol}} < 10^{-6}$ (Huenemoerder et al. 2015; Oskinova et al. 2012). Table 3 shows the range of -6.0 to -4.8 , which is well above the norm for single WR stars. The X-ray luminosities of the NGC 3603 stars also exceed the binary WR stars in the sample studied by Zhekov (2012), where only WR 148 approaches $L_x \sim 10^{34}$ ergs s⁻¹.

The O-type stars in our sample, MTT 68, MTT 71, and Sher 47 (see Table 1) are also highly luminous for their classes. Single O-stars also have $L_x/L_{\text{bol}} \sim 10^{-7}$ (Nazé et al. 2011). In a review of binary colliding winds, Rauw & Nazé (2016), from a variety of X-ray studies, conclude that X-ray bright colliding wind binaries are relatively rare; being in a binary does not necessarily confer high relative X-ray luminosity. Two early O-type stars in the core of NGC 3603, A2 and A3, have not been detected in X-rays though their bolometric luminosities are similar to the detected O-stars; perhaps they are “normal”, single systems. Whether the X-ray bright O-type systems in NGC 3603 are binary remains to be determined.

6. CONCLUSIONS

⁷ Townsley et al. (2014) source “p1_4736” is MTT 71.

The relatively short *Chandra*/HETG exposure has shown the feasibility of study of this cluster at high X-ray spectral resolution. For the brighter components which are saturated in ACIS imaging observations, we have provided more reliable flux measurements. We have confirmed the high terminal wind velocities in X-rays for HD 97950-A1, B, and C, and we have provided the first empirical estimates of the terminal velocities of MTT 68 and MTT 71 from X-ray line profiles. The high plasma temperatures and the very high values of L_x/L_{bol} strongly suggest a colliding winds origin for their X-rays.

Further studies of NGC 3603 stars in high resolution X-rays are needed to refine the characteristics of their winds and the origin of their very high X-ray luminosities. Higher signal-to-noise ratios are needed to determine emission line shapes in detail, as these are critical for measurement of the terminal velocity and of the optical depths in their winds. Higher signal is also needed to measure He-like line ratios of Mg XI and Si XIII, since these are sensitive to the UV radiation field and thereby serve as a proxy for distance of formation from the photospheres. Longer term X-ray studies are needed in order to search for variability expected from colliding wind binaries. Two of the systems, A1 and C, are known to be binaries and have relatively short periods, making them amenable to X-ray variability studies. Whether the other stars in this study are binaries remains to be determined and is important for interpretation of their properties.

Acknowledgements: Support for this work was provided by NASA through the Smithsonian Astrophysical Observatory (SAO) contract SV3-73016 to MIT for Support of the Chandra X-Ray Center (CXC) and Science Instruments. CXC is operated by SAO for and on behalf of NASA under contract NAS8-03060. We thank Prof. Claude Canizares for allocation of observing time for this observation from the HETG Guaranteed Time Observation Program.

Facility: CXO (HETG/ACIS)

Software: MARX (Davis et al. 2012), CIAO (Fruscione et al. 2006), ISIS (Houck & Denicola 2000)

REFERENCES

- Asplund, M., Grevesse, N., Sauval, A. J., & Scott, P., 2009, *ARA&A*, 47, 481
- Canizares, C. R., et al., 2005, *PASP*, 117, 1144
- Cassinelli, J. P., Miller, N. A., Waldron, W. L., MacFarlane, J. J., & Cohen, D. H., 2001, *ApJL*, 554, L55
- Cohen, D. H., Wollman, E. E., Leutenegger, M. A., Sundqvist, J. O., Fullerton, A. W., Zsargó, J., & Owocki, S. P., 2014, *MNRAS*, 439, 908
- Crowther, P. A., & Dessart, L., 1998, *MNRAS*, 296, 622
- Crowther, P. A., Schnurr, O., Hirschi, R., Yusof, N., Parker, R. J., Goodwin, S. P., & Kassim, H. A., 2010, *MNRAS*, 408, 731
- Davis, J. E., 2001, *ApJ*, 548, 1010
- Davis, J. E., et al., 2012, in *Space Telescopes and Instrumentation 2012: Ultraviolet to Gamma Ray*, Vol. 8443, 84431A
- Drissen, L., Moffat, A. F. J., Walborn, N. R., & Shara, M. M., 1995, *AJ*, 110, 2235
- Foster, A. R., Ji, L., Smith, R. K., & Brickhouse, N. S., 2012, *ApJ*, 756, 128
- Fruscione, A., et al., 2006, in *SPIE Conference Series*, Vol. 6270
- Gagné, M., Fehon, G., Savoy, M. R., Cartagena, C. A., Cohen, D. H., & Owocki, S. P., 2012, in *Proceedings of a Scientific Meeting in Honor of Anthony F. J. Moffat*, ed. L. Drissen, C. Robert, N. St-Louis, A. F. J. Moffat, Vol. 465, 301
- Gagné, M., Oksala, M. E., Cohen, D. H., Tonnesen, S. K., ud-Doula, A., Owocki, S. P., Townsend, R. H. D., & MacFarlane, J. J., 2005, *ApJ*, 628, 986
- Henley, D. B., Stevens, I. R., & Pittard, J. M., 2003, *MNRAS*, 346, 773
- Hofmann, K., Seggewiss, W., & Weigelt, G., 1995, *A&A*, 300, 403

- Houck, J. C., & Denicola, L. A., 2000, in *Astronomical Data Analysis Software and Systems IX*, ed. N. Manset, C. Veillet, & D. Crabtree, Vol. 216, 591
- Huenemoerder, D. P., et al., 2015, *ApJ*, 815, 29
- Ignace, R., 2001, *ApJL*, 549, L119
- Ignace, R., Gayley, K. G., Hamann, W.-R., Huenemoerder, D. P., Oskinova, L. M., Pollock, A. M. T., & McFall, M., 2013, *ApJ*, 775, 29
- Kahn, S. M., Leutenegger, M. A., Cottam, J., Rauw, G., Vreux, J.-M., den Boggende, A. J. F., Mewe, R., & Güdel, M., 2001, *A&A*, 365, L312
- Kramer, R. H., Cohen, D. H., & Owocki, S. P., 2003, *ApJ*, 592, 532
- Luo, D., McCray, R., & Mac Low, M., 1990, *ApJ*, 362, 267
- Maíz Apellániz, J., et al., 2016, *ApJS*, 224, 4
- Melena, N. W., Massey, P., Morrell, N. I., & Zangari, A. M., 2008, *AJ*, 135, 878
- Melnick, J., Tapia, M., & Terlevich, R., 1989, *A&A*, 213, 89
- Moffat, A. F. J., et al., 2002, *ApJ*, 573, 191
- Moffat, A. F. J., Drissen, L., & Shara, M. M., 1994, *ApJ*, 436, 183
- Moffat, A. F. J., Seggewiss, W., & Shara, M. M., 1985, *ApJ*, 295, 109
- Nazé, Y., et al., 2011, *ApJS*, 194, 7
- Oskinova, L. M., Feldmeier, A., & Hamann, W.-R., 2004, *A&A*, 422, 675
- Oskinova, L. M., Gayley, K. G., Hamann, W.-R., Huenemoerder, D. P., Ignace, R., & Pollock, A. M. T., 2012, *The Astrophysical Journal Letters*, 747, L25
- Owocki, S. P., & Cohen, D. H., 2001, *ApJ*, 559, 1108
- Pollock, A. M. T., & Corcoran, M. F., 2006, *A&A*, 445, 1093
- Pollock, A. M. T., Corcoran, M. F., Stevens, I. R., & Williams, P. M., 2005, *ApJ*, 629, 482
- Rauw, G., & Nazé, Y., 2016, *Advances in Space Research*, 58, 761
- Roman-Lopes, A., 2013, *MNRAS*, 435, L73
- Roman-Lopes, A., Franco, G. A. P., & Sanmartim, D., 2016, *ApJ*, 823, 96
- Romano, P., Campana, S., Mignani, R. P., Moretti, A., Mottini, M., Panzera, M. R., & Tagliaferri, G., 2008, *A&A*, 488, 1221
- Schnurr, O., Casoli, J., Chené, A., Moffat, A. F. J., & St-Louis, N., 2008, *MNRAS*, 389, L38
- Schulz, N. S., Canizares, C., Huenemoerder, D., & Tibbets, K., 2003, *ApJ*, 595, 365
- Stevens, I. R., Blondin, J. M., & Pollock, A. M. T., 1992, *ApJ*, 386, 265
- Stevens, I. R., Corcoran, M. F., & Moffat, A. F. J., 2002, in *Interacting Winds from Massive Stars*, ed. A. F. J. Moffat, N. St-Louis, Vol. 260, 343
- Stolte, A., Brandner, W., Brandl, B., & Zinnecker, H., 2006, *AJ*, 132, 253
- Townsley, L. K., Broos, P. S., Garmire, G. P., Bouwman, J., Povich, M. S., Feigelson, E. D., Getman, K. V., & Kuhn, M. A., 2014, *ApJS*, 213, 1
- van der Hucht, K. A., 2001, *NewAR*, 45, 135
- Zhekov, S. A., 2012, *MNRAS*, 422, 1332